Tuning Control Against Coupler Parameter Variations Due to Misalignment in an Optimal-Efficiency-Tracking and Constant-Power-Output IPT System

Bowei Zou, *Graduate Student Member, IEEE*, Zhicong Huang, *Senior Member, IEEE*, Io-Wa Iam, *Member, IEEE*, and Chi-Seng Lam, *Senior Member, IEEE*

***Abstract*—In inductive power transfer (IPT) systems, air gap variations can cause fluctuations in the parameters of the loosely coupled transformers (LCT), potentially compromising resonant tank performance, output stability, and transfer efficiency. To address this issue, this article introduces a novel multiloop control strategy for a single-stage power-source IPT system. Specifically, the proposed system replaces traditional compensation capacitors with switch-controlled capacitors on both sides and incorporates a semiactive rectifier on the secondary side. On this basis, a control strategy is identified and implemented with three loops, including a secondary tuning loop using a gradient descent method to counteract coupler parameter variations due to misalignment, a load matching loop for tracking optimal efficiency and a primary-side input impedance tuning loop for maintaining constant power output. This strategy maintains optimal efficiency and constant power output despite dynamic variations in LCT parameters, coupling coefficients, and load conditions. Notably, it eliminates the need for direct detection of LCT self-inductance and mutual inductance parameter variations. Furthermore, the system operates at a fixed frequency and achieves zero-voltage switching, enhancing overall efficiency. Finally, a 500 W experimental setup is established to validate the feasibility and effectiveness of the proposed system.**

***Index Terms*—Air gap variations, control loops, inductive power transfer (IPT), loosely coupled transformer (LCT) parameters, optimal efficiency.**

Received 26 June 2024; revised 15 November 2024; accepted 31 December 2024. Date of publication 3 January 2025; date of current version 26 February 2025. This work was supported in part by the Science and Technology Planning Project of Guangdong Province under Grant 2023A0505050124, in part by the Natural Science Foundation of Guangdong Province under Grant 2023A1515011623, in part by the Guangzhou Municipal Science and Technology Bureau under Grant 2025A04J7064, in part by the Science and Technology Development Fund, Macau SAR (FDCT), under Grant 0027/2021/A1, 0015/2022/AMR and Grant 004/2023/SKL, and in part by the University of Macau under Grant MYRG-GRG2024-00086-IME and Grant MYRG-GRG2023-00167-IME. Recommended for publication by Associate Editor C. Fernandez. *(Corresponding authors: Zhicong Huang; Io-Wa Iam.)*

Bowei Zou, Zhicong Huang, and Io-Wa Iam are with the Shien-Ming Wu School of Intelligent Engineering, South China University of Technology, Guangzhou 510006, China (e-mail: zhiconghuang@scut.edu.cn).

Chi-Seng Lam is with the State Key Laboratory of Analog and Mixed-Signal VLSI, University of Macau, Macau 999078, China, also with the Institute of Microelectronics, University of Macau, Macau 999078, China, and also with the Department of Electrical and Computer Engineering, Faculty of Science and Technology, University of Macau, Macau 999078, China (e-mail: cslam@um.edu.mo).

Color versions of one or more figures in this article are available at https://doi.org/10.1109/TPEL.2025.3525515.

Digital Object Identifier 10.1109/TPEL.2025.3525515

I. Introduction

WIRELESS power transfer (WPT) technology utilizes electromagnetic fields as a transmission medium and is based on the principle of electromagnetic induction to achieve contactless transfer of energy from the power supply to the load [1], [2]. Among these technologies, inductive power transfer (IPT) has been widely applied in electric vehicles (EVs), automatic guided vehicles (AGVs) and other fields due to its advantages in safety, flexibility, and reliability [3], [4], [5], [6], [7], [8], [9], [10], [11], [12]. In practical scenario, the chassis height of EVs and AGVs inevitably fluctuates due to changes in load weight [13], [14]. These fluctuations directly affect the air gap between coupling coils in IPT systems. Such variations in air gap lead to significant alterations in both the mutual inductance and self-inductance of loosely coupled transformers (LCT), which directly impacts the output performance of the system. Fig. 1(a) illustrates the typical LCT employed in the IPT system. For simplicity, the primary and secondary sides adopt the same single-layer circular structure with ferrite cores. The corresponding relationship between LCT parameters and the air gap d is depicted in Fig. 1(b). As the air gap d increases from 20 mm to 80 mm, significant trends emerge that self-inductances (L_P and L_S) show a gradual decrease, while mutual inductance M and coupling coefficient k exhibit substantial reductions. Due to the complications caused by misalignment uncertainty, the difficulty of resonant tuning of IPT systems is greatly increased. Without an effective resonance tuning solution, IPT systems are prone to reduced power transfer efficiency and unstable output, compromising the overall performance and reliability.

To maintain the resonance state of the IPT system with different air gaps, researchers have explored various tuning methods classified into two main categories: passive strategies and active control strategies. In passive strategies, including magnetic coupler design [15], compensation network [16], [17], and parameter optimization [18], [19]. The aforementioned passive strategies demonstrate some efficacy in mitigating efficiency decline and output fluctuations caused by air gap variations within a limited range. However, maintaining precise output characteristics over a wider range of air gap and load variations remains a major challenge. To address this weakness, active control

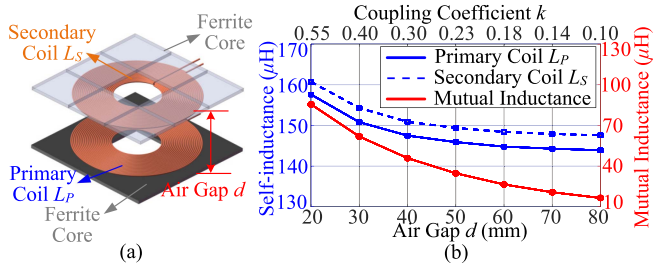

Fig. 1. Typical LCT and its parameters versus the air gap d. (Unless specified, they will be used for the rest simulation.) (a) Typical coupling pad of the IPT system. (b) Profile of the LCT parameters versus the air gap d.

strategies, such as phase shifting control or frequency tracking controls, are commonly employed in IPT systems to counteract mismatches caused by air gap variations [20], [21], [22]. In [20], by employing inverter phase-shifting control combined with the adjustable system input impedance resulting from LCT self-inductance variations, constant current output and a wider range of zero voltage switching (ZVS) can be achieved. However, this approach may encounter control instability issues during deep modulation, potentially leading to increased inverter losses and reduced system efficiency. On the other hand, frequency tracking strategies dynamically adjust the switching frequency based on primary-side phase information, using techniques such as phase-locked loops (PLLs) to maintain resonance [21], [22]. However, variations in overall LCT parameters constrain the bandwidth of the system's operating frequency. Furthermore, the challenges associated with active tuning of the secondary side can also impact system efficiency.

To improve overall tuning control of the system, impedance tuning control is increasingly being employed to address the detuning problem of IPT system. By employing variable impedance components such as capacitor matrices [23], variable inductors [24], [25], and switch-controlled capacitors (SCCs) [26], [27], [28], [29], [30], the impedance is adjusted to compensate for the detuning effects caused by air gap variations in IPT systems. A (M $\times$ N) capacitance matrix is proposed, which allows for flexible changes in capacitance values [23]. However, increasing the number of capacitors and switches to achieve the desired tuning range and precision inevitably leads to increased system size and cost. In [24], a winding coil is added to the magnetic core, and a variable reactance is realized by controlling the dc bias voltage. However, this approach may encounter certain issues such as magnetic core saturation, noise, and electromagnetic compatibility concerns, especially in cases of significant self-inductance variation [25].

The SCC, comprising individual capacitors connected to MOSFETs, has emerged as another method for compensating detuning in IPT systems [26]. For instance, the SCC in [27] is utilized to cancel undesired reactance generated by semi-active rectifiers (SAR), maintaining resonance conditions in the secondary side. Regretfully, while this approach maintains constant power output with optimal transfer efficiency under load changes, it struggles to address dynamic coupler parameter variations or misalignment issues. In [28], the self-tuning of *LCC* compensation topology is achieved by actively controlling the SCCs using pulsewidth modulation (PWM). However, this approach primarily addresses the issue of self-inductance variation on the primary side, with secondary side detuning still leading to decreased system efficiency. In [29], SCCs are implemented at both the transmitter and the receiver, enabling dual-side self-tuning through methods to estimate inductance and mutual inductance parameters. Yet, the complex parameter identification process may not suit scenarios with real-time coupling parameter changes. In [30], the IPT system employs SCCs on both sides simultaneously to maintain constant power output despite changes in self-inductance and mutual inductance. Nevertheless, this approach may struggle to maintain optimal efficiency tracking when load conditions change concurrently. Consequently, achieving and sustaining optimal efficiency tracking and constant power output in IPT systems remains a significant challenge, especially in the presence of dynamic air gap variations (i.e., variations in both self-inductance and mutual inductance of the LCT) alongside varying load conditions.

To address the abovementioned challenge of IPT systems, this article proposes a decoupled multiloop control based on a single-stage power-source IPT system, which effectively eliminate the need for detecting variations in LCT parameters. The proposed decoupled multiloop control strategy comprises three key parts including a gradient descent method for secondary tuning control, load matching for optimal efficiency tracking control, and primary input impedance tuning for constant power output. This comprehensive approach enables the system to maintain optimal efficiency and constant power output even under simultaneous variations in self-inductance, mutual inductance, and load conditions. Furthermore, the design ensures that all power switches operate at a fixed frequency and achieve ZVS, thereby reducing switch losses.

The rest of this article is organized as follows. In Section II, the IPT system topology is presented, followed by an analysis of the operating principle of SAR and SCC for achieving soft switching. An efficiency analysis of the system is conducted based on the equivalent circuit model of the system. Section III-D provides a detailed explanation of the proposed decoupled multiloop control against coupler parameter variations due to air gap, including gradient descent method for secondary tuning control loop, load matching for tracking optimal efficiency control loop, and primary input impedance tuning for constant power output control loop. In Section IV, experimental results are obtained from a 500 W prototype to validate the proposed system and control loops. Finally, Section V concludes this article.

II. Operating Principle and Analysis of the IPT System

Fig. 2 shows the circuit topology of an IPT system with variable LCT parameters based on two SCCs and a SAR. As usual, the LCT has primary self-inductance L_P, secondary self-inductance L_S, and mutual inductance M. The coupling coefficient is defined as $k = \frac{M}{\sqrt{L_P L_S}}$. R_P and R_S denote equivalent series resistors, representing in the primary and secondary circuits, respectively. Instead of conventional compensation capacitors, switch-controlled capacitor $C_{P,\mathrm{SCC}}$ and $C_{S,\mathrm{SCC}}$ are

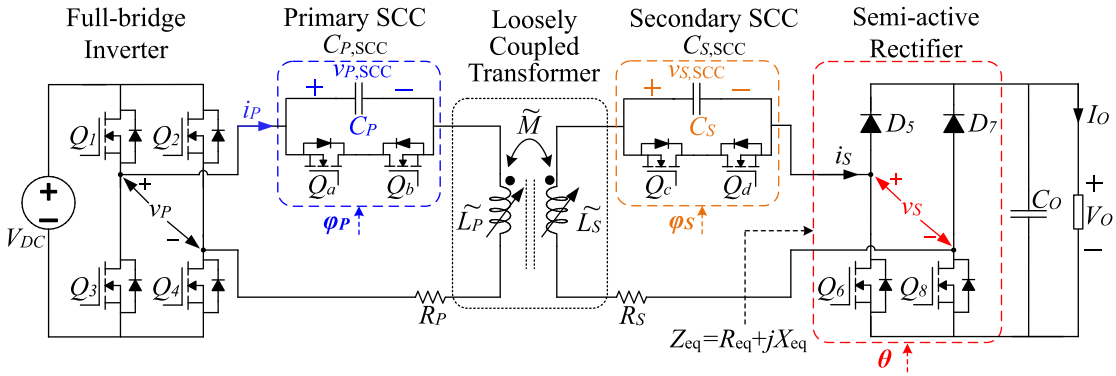

Fig. 2. Circuit topology of variable LCT parameters IPT system with two SCCs and a SAR.

used on both the primary and secondary sides, respectively. The SCC consists of a fixed-value capacitor and two MOSFET switches. Here, v_{SCC} represents the terminal voltage of the switch-controlled capacitor. High-frequency ac voltage v_P drives the primary coil through a full bridge inverter comprising four MOSFETs Q_1–Q_4. The angular frequency of the system is $\omega = 2\pi f = \frac{1}{\sqrt{L_P C_P}} = \frac{1}{\sqrt{L_S C_S}}$, where f represents the switching frequency of the inverter. The SAR on the secondary side consists of two diodes D_5 and D_7 in the upper legs, and two MOSFET switches Q_6 and Q_8 in the lower legs. The secondary side voltage v_S and current i_S represent the input ac voltage and current of the SAR, respectively. C_O represents the output filter capacitor. I_O and V_O, respectively, denote the output current and voltage of the dc load R_L.

A. Soft-Switched Modulations and Models of SAR and SCC

The modulations of the SAR has been studied in [31] and [32]. Q_6 and Q_8 are utilized to modulate θ, representing the conduction angle of v_S. They are turned ON during the conduction period of their antiparallel diodes to achieve ZVS. They operate complementarily within a single PWM cycle, each conducting for only half of the cycle. It should be noted that the conduction angle θ of the SAR ranges from 0 to a maximum π, i.e., $\theta \in [0, \pi]$ and will affect the phase difference between v_S and i_S. Therefore, employing this modulation technique can effectively equate the input impedance of the SAR to the impedance required by the converter. However, its equivalent load is an impedance $Z_{\mathrm{eq}} = R_{\mathrm{eq}} + jX_{\mathrm{eq}}$, rather than the usual pure resistance. Here, $R_{\mathrm{eq}} = \frac{8}{\pi^2} R_L \sin^4(\frac{\theta}{2})$, and $X_{\mathrm{eq}} = -\frac{8}{\pi^2} R_L \sin^3(\frac{\theta}{2}) \cos(\frac{\theta}{2})$.

The concept of SCC was first proposed in [33]. Its operational principle involves controlling the charging and discharging durations of the capacitor by adjusting the control angle φ, allowing it to vary continuously within a defined range [27]. Given that the operational principles of the primary and secondary SCCs are identical, the secondary SCC is selected as an illustrative example to elucidate its operational mechanism. When i_S enters its positive half-cycle, Q_d is turned OFFafter a time delay of $\varphi_S \in [\frac{\pi}{2}, \pi]$, causing Q_c to turn ON and remain conducting through the next zero-cross point, resulting in i_S transitioning from positive to negative. Subsequently, Q_d is turned ON after a delay of φ_S and remains active for half a PWM cycle. It is evident that when the MOSFET is turned ON, $v_{S,\mathrm{SCC}}$ remains zero, thus enabling ZVS operation of the SCC to reduce switch losses. It has been studied that $C_{S,\mathrm{SCC}}$ can be calculated by considering the fundamental components of i_S and $v_{S,\mathrm{SCC}}$ [27]. The capacitive reactance donated by $C_{S,\mathrm{SCC}}$ is highlighted as follows:

$$C_{S,\mathrm{SCC}} = \frac{C_S}{2 - \frac{2\varphi_S - \sin 2\varphi_S}{\pi}} \approx \frac{\pi^2}{4(\varphi_S - \pi)^2} C_S. \tag{1}$$

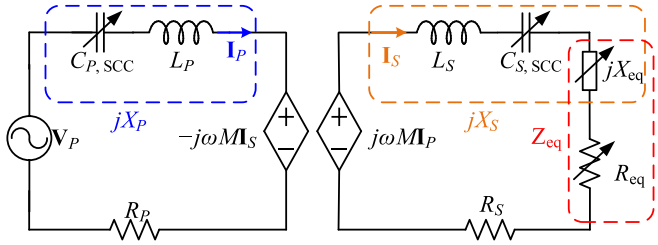

Fig. 3. Equivalent circuit model of the proposed system.

B. Equivalent Circuit Model

An equivalent circuit model of the proposed system using the fundamental approximation is shown in Fig. 3. In the topology, the switch-controlled capacitor $C_{P,\mathrm{SCC}}$ on the primary side and $C_{S,\mathrm{SCC}}$ on the secondary side, along with the load Z_{eq}, are all controllable variables. v_p, i_p, v_s, and i_s are fundamental components, and $\mathbf{V}_P$, $\mathbf{I}_P$, $\mathbf{V}_S$, and $\mathbf{I}_S$ are vector representation of fundamental components, respectively. The resistance R_P represents the parasitic resistance from the inverter, the primary SCC, and the primary coil. Similarly, resistor R_S accounts losses arising from the secondary coil, the secondary SCC, and the SAR. Applying Kirchhoff 's voltage law to the equivalent circuit model, the relationship can be expressed as follows:

$$\mathbf{V}_P - (jX_P + R_P)\mathbf{I}_P = -jX_M\mathbf{I}_S, \text{ and} \tag{2}$$

$$jX_M\mathbf{I}_P = (jX_S + R_S + R_{\mathrm{eq}})\mathbf{I}_S. \tag{3}$$

where

$$X_P = \omega L_P - \frac{1}{\omega C_{P,\mathrm{SCC}}} \tag{4}$$

$$X_S = \omega L_S - \frac{1}{\omega C_{S,\mathrm{SCC}}} + X_{\mathrm{eq}}, \text{ and} \tag{5}$$

$$X_M = \omega M. \tag{6}$$

C. Efficiency Analysis

Assuming the system is operating in a steady-state condition, and based on the equivalent circuit depicted in Fig. 3, the power transfer efficiency η is defined as the ratio of the output active power to the input active power, given as follows:

$$\eta = \frac{|\mathbf{I}_S|^2 R_{\mathrm{eq}}}{|\mathbf{I}_S|^2 (R_{\mathrm{eq}} + R_S) + |\mathbf{I}_P|^2 R_P} \tag{7}$$

$$= \frac{X_M^2 R_{\mathrm{eq}}}{[(R_{\mathrm{eq}} + R_S)^2 + X_S^2] R_P + X_M^2 (R_{\mathrm{eq}} + R_S)}. \tag{8}$$

As a high-quality IPT system usually satisfies $\frac{X_M^2}{R_P R_S} \gg 1$ and $\frac{R_{\mathrm{eq}}}{R_S} \gg 1$ [32], η can be further simplified as follows:

$$\eta \approx \frac{1}{\frac{R_{\mathrm{eq}} + \frac{X_S^2}{R_{\mathrm{eq}}}}{X_M^2} R_P + \frac{R_S}{R_{\mathrm{eq}}} + 1}. \tag{9}$$

To achieve the optimal power transfer efficiency, the optimum values of R_{eq} and X_{S} can be determined from (9). If the operating frequency ω remains constant, achieving optimal efficiency η_{opt} involves solving the partial derivatives $\frac{\partial \eta}{\partial X_S} = 0$ and $\frac{\partial \eta}{\partial R_{\mathrm{eq}}} = 0$, given as follows:

$$\eta_{\mathrm{opt}} \approx \frac{1}{\frac{2}{\frac{X_M}{\sqrt{R_P R_S}}} + 1}, \text{ if} \tag{10}$$

$$X_{S,\mathrm{opt}} = \omega L_S - \frac{1}{\omega C_{S,\mathrm{SCC}}} + X_{\mathrm{eq}} = 0, \text{ and} \tag{11}$$

$$R_{\mathrm{eq,opt}} = X_M \sqrt{\frac{R_S}{R_P}}. \tag{12}$$

The optimal transfer efficiency criteria, as outlined in (11) and (12), indicate two crucial conditions including the secondary resonant tank should maintain a null equivalent reactance, and the equivalent load should be matched to its optimal value. In addition, it is noted that primary equivalent reactance X_P does not contribute to an increase in the voltage-ampere capacity of the IPT system, nor does it negatively impact efficiency performance. These principles form the foundation of the control strategy proposed in this article, and the detailed implementation methods for this strategy are elaborated in Section III-D.

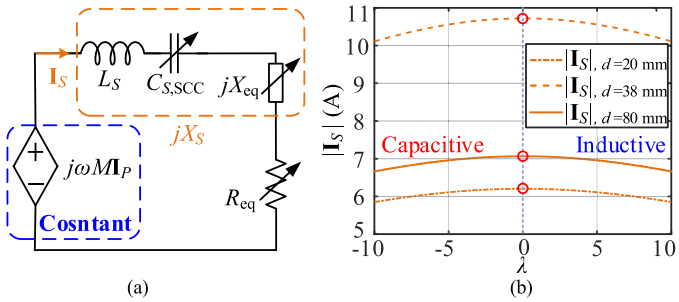

Fig. 4. Principle of secondary tuning control. (a) Secondary side equivalent circuit. (b) Secondary side current $|\mathbf{I}_S|$ versus reactance per-unit value λ.

III. Proposed Multiloop Control and Principle

A. Gradient Descent Method for Secondary Tuning Against Coupler Parameter Variations Due to Misalignment

As shown in Fig. 1, variations in the air gap lead to changes in the secondary self-inductance L_S within a defined range. According to (5), the change of L_S will affect the reactance of the secondary side. To satisfy one of the conditions for optimal transfer efficiency, as stipulated in (11), comprehensive compensation of the secondary self-inductance L_S is required to maintain resonance. However, real-time detection of the parameter variations in L_S poses significant challenges during practical circuit operation. Therefore, this article proposes a secondary tuning inner control loop that eliminates the need for detecting changes in LCT parameters. Benefiting from the higher control frequency of the inner loop, at this stage, the primary current $\mathbf{I}_P$ can be treated as constant. Consequently, the simplified equivalent circuit of the secondary side, as shown in Fig. 4(a), depicts a constant voltage source $j\omega M\mathbf{I}_P$. The secondary side can be regarded as an independent circuit with a constant voltage source, allowing for separate tuning processes and thus achieving decoupled control between the primary and secondary sides.

For a more intuitive analysis of the impact of varying the self-inductance L_S on the secondary reactance. Combined with (5), λ is defined as the per-unit value of the secondary side reactance corresponding to different air gaps, given as follows:

$$\lambda = \frac{X_{S,\mathrm{var.}}}{\omega L_{S,0} - \frac{1}{\omega C_S} + X_{\mathrm{eq}}} \tag{13}$$

where $L_{S,0}$ is the self-inductance value under the different air gaps. Furthermore, the reactance X_S directly influences the magnitude of the secondary-side current $|\mathbf{I}_S|$. With reference to the equivalent circuit depicted in Fig. 4(a), the magnitude of the secondary-side current $|\mathbf{I}_S|$ is given as follows:

$$|\mathbf{I}_S| = \frac{\omega M |\mathbf{I}_P|}{\sqrt{\lambda^2 + R_{\mathrm{eq}}^2}}. \tag{14}$$

As shown in Fig. 4(b), $|\mathbf{I}_S|$ is plotted versus the secondary reactance per-unit value λ for different air gaps d reveals that the amplitude $|\mathbf{I}_S|$ decreases when the secondary reactance is capacitive or inductive. In addition, the maximum value of $|\mathbf{I}_S|$

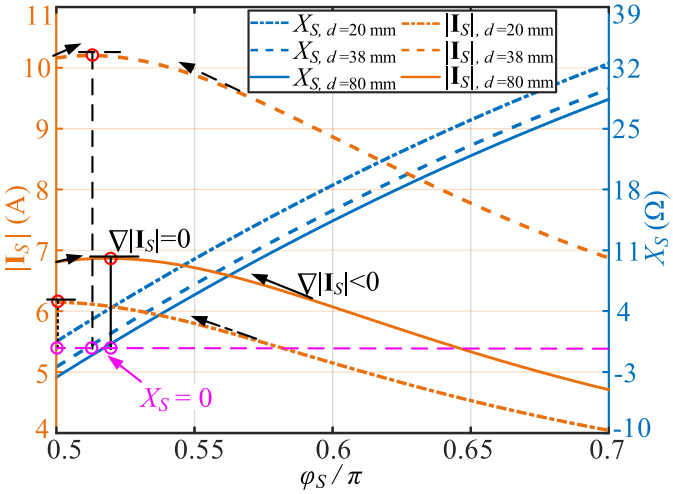

Fig. 5. X_S and $|\mathbf{I}_S|$ versus secondary SCC control angle φ_S under different air gaps.

is only reached when the $\lambda = 0$. This means that the optimum resonance state of the secondary side can be determined by identifying the point of maximum value of $|\mathbf{I}_S|$ to satisfy (11). Combined with (1), (5), (13), (14), and (15) can be obtained, the amplitude $|\mathbf{I}_S|$ is regulated by the control angle φ_S of the secondary SCC.

$$|\mathbf{I}_S| = \frac{\omega M |\mathbf{I}_P|}{\sqrt{\left(\omega L_{S,0} - \frac{1}{\omega \frac{\pi^2}{4(\varphi_S-\pi)^2} C_S} + X_{\text{eq}}\right)^2 + R_{\text{eq}}^2}}. \quad (15)$$

As an illustration, monotonic curves of $|\mathbf{I}_S|$ and X_S versus φ_S for various values of air gap are shown in Fig. 5. It can be observed that the objective function $|\mathbf{I}_S|$ (φ_S) is a nonlinear function with the secondary SCC control angle φ_S as the independent variable. Hence, this article proposes the utilization of a gradient descent method to search for the maximum value of the $|\mathbf{I}_S|$. The principle of gradient descent involves iteratively searching along the gradient direction of the objective function until the extremum of the objective function is found. As shown in Fig. 5, the gradient of the objective function $|\mathbf{I}_S|$ is as follows:

$$\nabla |\mathbf{I}_S| = \frac{\Delta |\mathbf{I}_S|}{\Delta \varphi_S}. \quad (16)$$

From (16), the optimal iterative equation of the objective function $|\mathbf{I}_S|$ can be obtained as follows:

$$(|\mathbf{I}_S|, \varphi_S)_{i+1} = (|\mathbf{I}_S|, \varphi_S)_i + \beta(\nabla |\mathbf{I}_S|)_i. \quad (17)$$

where i represents the iteration count; $(|\mathbf{I}_S|, \varphi_S)_k$ denotes the initial values at the kth iteration; $(|\mathbf{I}_S|, \varphi_S)_{k+1}$ represents the updated $|\mathbf{I}_S|$ and φ_S values after the $(k+1)$th iteration; β denotes the iteration step size, also referred to as the learning rate. Feedback control of the secondary SCC is achieved by iteratively detecting the magnitude of the secondary side current $|\mathbf{I}_S|$. The termination criterion for the iteration is reached when the magnitude of the gradient vector of (16) approaches 0. At this point, $|\mathbf{I}_S|$ reaches its maximum value (indicated by the orange curves), and X_S (indicated by the blue curves) is also equal 0. This indicates that the secondary side is in resonance, and enables the realization of tuning control of the secondary side.

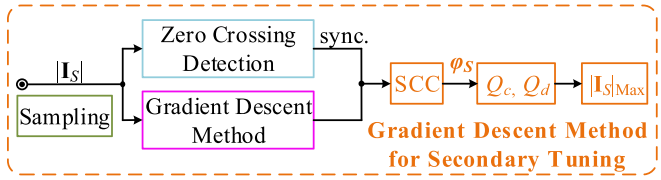

Fig. 6. Control diagram of gradient descent method for secondary tuning.

The control diagram for secondary tuning control loop is depicted in Fig. 6. Current sampling is responsible for measuring the amplitude of the secondary resonant tank currents i_S. Then, zero crossing detection (ZCD) of i_S generates the PWM synchronous trigger signal for the secondary SCC, with the corresponding drive signals are transmitted as Q_c and Q_d. The amplitude $|\mathbf{I}_S|$ is continuously detected, and the value of φ_S is continuously adjusted by the gradient descent method to ensure that $|\mathbf{I}_S|$ remains at its maximum value throughout the control period. This ensures that even when the secondary side self-inductance L_S fluctuates, the secondary side remains in resonance, satisfying one of the conditions for optimal transfer efficiency tracking.

B. Load Matching for Optimal Efficiency Tracking

The secondary SAR optimal load matching is used as the middle loop control, with the aim of achieving optimal load matching under the null equivalent reactance state achieved in the inner loop, so as to further optimize the transfer efficiency of the system. Form (12), the optimal load $R_{\text{eq,opt}}$ is a variable dependent on the magnetic coupling coefficient. To make (12) valid, it is an intuitive need to continuously detect the air gap for perceiving and tracking the optimal load value in practical applications, thus significantly increasing implementation complexity and challenges. In this article, a viable condition is explored for optimizing efficiency that is equivalent to (12) but decoupled from the air gap. By satisfying the null secondary reactance, i.e., $X_S = X_{S,\text{opt}} = 0$, and substituting (11) into (3), the ratio α of the amplitude of the secondary current $|\mathbf{I}_S|$ to the amplitude of the primary current $|\mathbf{I}_P|$ can be defined as follows:

$$\alpha = \left|\frac{\mathbf{I}_S}{\mathbf{I}_P}\right| = \frac{X_M}{(R_{\text{eq}} + R_S)}. \quad (18)$$

From (18), it is evident that the variables affecting the current ratio α include the air gap and the equivalent load. In comparison to the equivalent resistance R_{eq}, the secondary resistance R_S is relatively small and can be neglected. With (7) and (18), typical curves of efficiency η versus current ratio α are plotted in Fig. 7(a). It is apparent that there are efficiency peaks under different values of air gap d. By substituting $X_{S,\text{opt}}$ and $R_{\text{eq,opt}}$ given by (11) and (12) into (3), the optimal α_{opt} can be derived

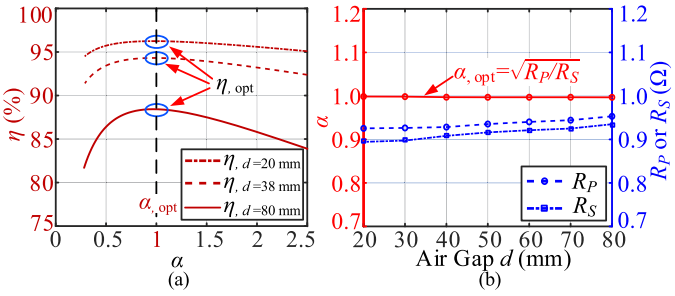

Fig. 7. Principle of load matching control. (a) Efficiency η versus current ratio α under different values of k. (b) Current ratio α and $R_P(R_S)$ versus air gap d. (Unless specified, they will be used for the rest simulation.)

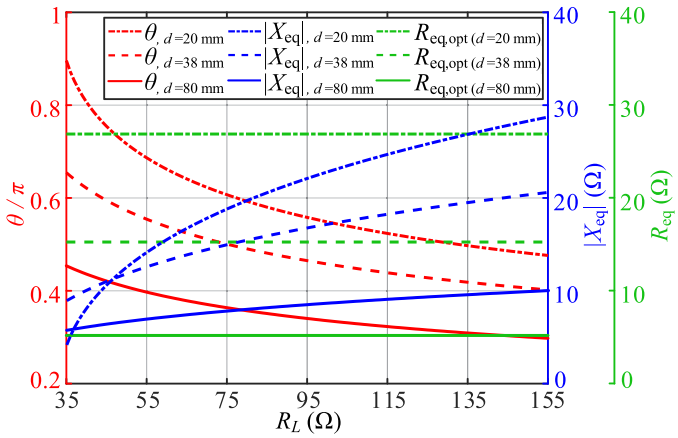

Fig. 8. Conduction angle θ of the SAR, X_{eq} versus load R_L.

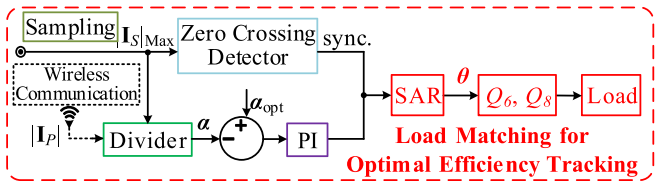

Fig. 9. Control diagram of load matching for optimal efficiency tracking.

as follows:

$$\alpha_{\text{opt}} = \left|\frac{\mathbf{I}_S}{\mathbf{I}_P}\right| \approx \sqrt{\frac{R_P}{R_S}}. \tag{19}$$

From (19), it demonstrates that the optimal current ratio α_{opt} is a equivalent condition for optimizing system efficiency to (12). Importantly, α_{opt} is solely dependent on the equivalent resistances of the primary and secondary sides, but independent of the air gap. As shown in Fig. 7(a), maintaining α at α_{opt} consistently enables the IPT system to operate at optimal efficiency across varying air gap d. In practical applications, α_{opt} is mainly influenced by resistances R_P, R_P and losses from all switching devices. Therefore, it is essential to evaluate α_{opt} based on the experimentally measured parameters. With the experimental parameters detailed in Section IV, Fig. 7(b) shows that the ratio $\alpha = \sqrt{\frac{R_P}{R_S}}$ remains approximately 1.0 as the air gap d varies. Hence, using $\alpha_{\text{opt}} = 1.0$ as a control reference is appropriate. To ensure that the actual load R_L matches the optimal load $R_{\text{eq,opt}}$ regardless of air gap variations, the conduction angle θ of the SAR is adjusted. The partial differential in (20) reveals that α decreases steadily as θ increases, allowing for the use of a linear controller to regulate θ.

$$\frac{\partial \alpha}{\partial \theta} = -\frac{\pi^2 \omega_0 M}{16 R_L \sin^5(\frac{\theta}{2})} \cos\left(\frac{\theta}{2}\right) < 0, \text{ for } \theta \in [0, \pi]. \tag{20}$$

Fig. 8 illustrates the variations in the controlled variables θ, X_{eq}, and $R_{\text{eq,opt}}$ under different d within the range of load R_L variations. The red curves represent variations of θ with respect to R_L. The green lines indicate that, by controlling θ of the SAR to maintain the optimal current ratio α_{opt}, the equivalent load value consistently remains at the optimal load $R_{\text{eq,opt}}$ under different d. The blue curves illustrate the absolute value of X_{eq} generated by modulating θ with the SAR.

The load matching control block diagram is shown in Fig. 9. This control strategy optimizes the transfer efficiency by maintaining the optimal current ratio α_{opt}. It employs amplitude sampling circuits to measure primary and secondary currents, with wireless communication transmitting the primary current value to the secondary side. It is noteworthy that the proposed control scheme relies solely on amplitude data, while precise phase detection of the high-frequency current is not needed. Thus, a simple PI controller is employed to correct any deviation from α_{opt}, ensuring the equivalent load matches the optimal load. Then, the control signal θ for the SAR is generated by this PI controller, corresponding to the drive signals that operate Q_6 and Q_8. Finally, similarly to operation of secondary SCC, the ZCD of i_S generates a PWM synchronization signal for the SAR to complete the optimal load matching control.

C. Primary Input Impedance Tuning for Constant Power Output

When variations occur in the air gap and load, besides impacting transmission efficiency, it also has serious damage to the transmission power. Therefore, in dynamic IPT, a wide range of output power is necessary to ensure compliance with the output requirements of the load under parameter fluctuations. Based on the optimal efficiency transmission control loop on the secondary side, we have similarly employed SCC on the primary side and proposed a decoupled outer regulated power control loop. The primary input impedance is utilized to maintain a wide range of output power, ensuring the stability of the system output. Assuming $R_P = R_S = 0$, i.e., lossless power transfer, the output power can be derived with (2), (3), (11), and (12), and it is given as follows:

$$P_O = \left|\frac{\mathbf{I}_S}{\sqrt{2}}\right|^2 R_{\text{eq,opt}} = \frac{|\mathbf{V}_P|^2 X_M}{2(X_P^2 + X_M^2)}. \tag{21}$$

From (21), when the operating frequency of the system is fixed, the output power P_O can be controlled only by changing the value of the primary input impedance X_P. The modulation of the primary SCC is similar to that of the secondary SCC, hence it would not be reiterated here. The equivalent capacitance of

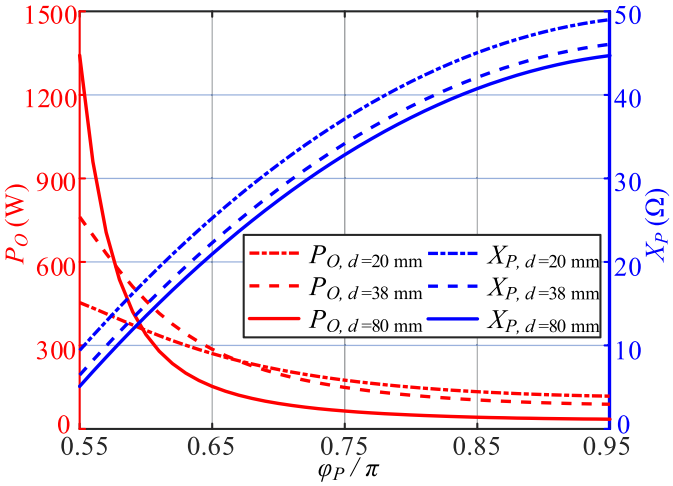

Fig. 10. Output power P_O versus primary SCC control angle φ_S.

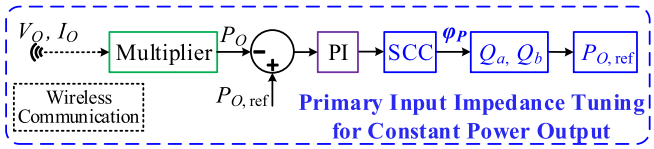

Fig. 11. Control block diagram of primary input impedance tuning for constant power output.

the primary SCC is given by (22), where φ_P is the control angle of the primary SCC.

$$C_{P,\text{SCC}} \approx \frac{\pi^2}{4(\varphi_P-\pi)^2}C_P. \tag{22}$$

Hence, the primary input impedance X_P can be calculated as follows:

$$X_P = \omega L_P - \frac{4(\varphi_P-\pi)^2}{\pi^2\omega C_P}. \tag{23}$$

The relationship between the control angle φ_P of the primary SCC and the output power can be further investigated by solving the partial differential (24). Fig. 10 shows the simulated curves of P_O and X_P versus φ_P under different air gaps. The red curves represent that P_O decreases monotonously with the increase of φ_P, while the blue curves are the corresponding X_P. Therefore, φ_P should be tightly regulated by another PI controller to ensure the constant output power of the system when the air gap and the load condition vary.

$$\frac{\partial P_O}{\partial \varphi_P} = \frac{8V_p^2 X_P X_M(\varphi_P-\pi)}{\omega\pi^2 C_P(X_P^2+X_M^2)^2} < 0, \text{ for } \varphi_P \in [\pi/2, \pi]. \tag{24}$$

The control diagram for regulating output power of the primary SCC is shown in Fig. 11. The dc values of the output voltage V_O and the output current I_O are obtained by the dc sampling circuit. Wireless communication is used to send to the primary side, and the actual output power P_O of the system is obtained through a multiplier. The difference between P_O and

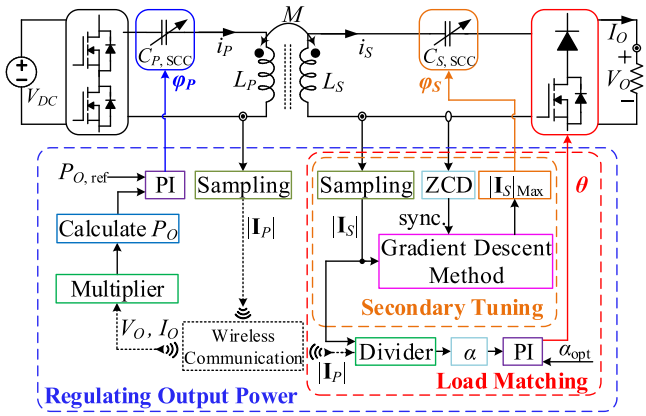

Fig. 12. Control diagram of the proposed multiloop control.

$P_{O,\text{ref}}$ can be corrected by a simple PI controller and the control angle φ_P is generated to drive the Q_a and Q_b of the primary side SCC.

D. Implementation of Proposed Mutiloop Control

Following the abovementioned analysis, the proposed multiloop control strategy is depicted in Fig. 12. First of all, for the secondary tuning (inner loop), an amplitude sampling circuit measures the secondary current $|\mathbf{I}_S|$. Using a gradient descent method, the system identifies $|\mathbf{I}_S|_{\text{Max}}$, determining the optimal control angle φ_S for the secondary SCC. This ensures the secondary circuit maintains a null equivalent reactance state. Afterwards, for the load matching (middle loop), the primary current amplitude $|\mathbf{I}_P|$ is wirelessly transmitted to the secondary side, where the actual current ratio α is calculated. A PI controller adjusts the conduction angle θ of the secondary SAR to regulate α to α_{opt}, achieving optimal load matching and efficiency tracking. Then, for the power control (outer loop), operating at a lower frequency than the secondary loops, this primary-side control ensures the completion of secondary-side optimization before each update. The dc values of V_O and I_O are sampled on the secondary side, with their product P_O wirelessly transmitted to the primary side. A PI controller corrects the difference between P_O and its reference $P_{O,\text{ref}}$, generating the control angle φ_P for the primary SCC.

IV. Experimental Results

A 500 W experimental prototype is built to verify the proposed topology and control strategy, as displayed in Fig. 13. The experimental prototype includes a full-bridge inverter, primary SCC, LCT, secondary SCC, secondary SAR, sampling circuits, and control circuits. Detailed system parameters are provided in Table I. The primary side pad is fixed, while the air gap of the secondary side pad relative to the primary side pad can be adjusted by rotating the rocker. The air gap varies within the range of 20 to 80 mm, corresponding to the coupling coefficient k ranging from 0.1 to 0.55. The magnitude of self-induced varies on the primary and secondary sides is shown in Fig. 1(b). Electronic loads are utilized to simulate the equivalent resistance,

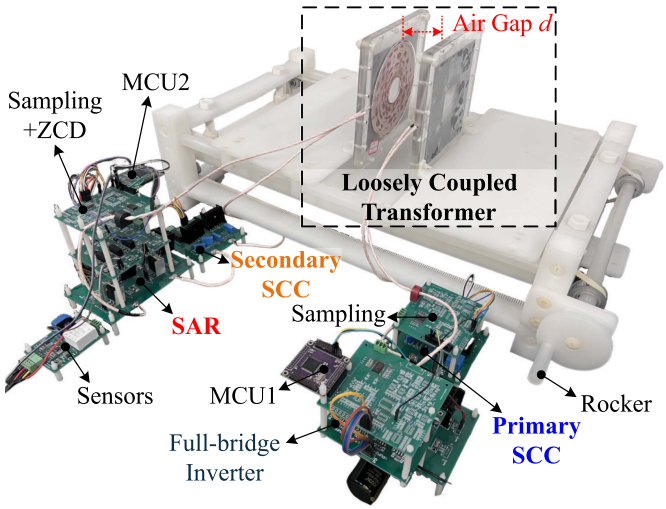

Fig. 13. Experimental prototype.

TABLE I
EXPERIMENTAL PARAMETER VALUES

Parameters	Symbols	Measured Values
Input voltage	V_{DC}	130 V
Number of turns	N	34
Inner diameter	d_i	40 mm
Outer diameter	d_o	150 mm
Primary self inductance	L_P	143.9–157.6 μH
Secondary self inductance	L_S	147.6-160.7 μH
Primary coil resistance	$R_{P,w}$	0.376–0.379 Ω
Secondary coil resistance	$R_{S,w}$	0.370–0.374 Ω
Coupling coefficient	k	0.1–0.55
Air gap distance	d	20–80 mm
Primary compensation	C_P	62.9 nF
Secondary compensation	C_S	63.7 nF
Operating frequency	$\frac{\omega}{2\pi}$	50 kHz
Load	R_L	35–155 Ω

with a range of 35 to 155 Ω. The MOSFETs (SCT4050DR) are used as the switches Q_1–Q_4, Q_6, Q_8, Q_a–Q_d, and Schottky diode (ASD2065P2) is used as D_5 and D_7.

A. Comparison of Steady-State Experimental Results

Two sets of comparative experiments are performed under different air gaps to demonstrate that the effectiveness of the proposed topology and multiloop control method in tracking the optimal efficiency and maintaining stable output. One set of experimental results is obtained without controlling (the traditional S/S compensation IPT), as depicted in Fig. 14, while the other set is obtained after controlling (based on the proposed topology and control strategy), as shown in Fig. 15. Under the same load ($R_L = 35\ \Omega$), the operating waveform of the topology without control is first captured under the condition of $d =$ 20–80 mm, as shown in Fig. 14. Comparing Fig. 14(a) with (b) and (c), with the air gap increases, the phase of the i_P (green curves) is ahead of the v_P (red curves), and the primary side is capacitive. Meanwhile, the phase difference between the i_P and the i_S (magenta curves) cannot be maintained to be 0.5π, resulting in detuning on both sides, which will cause additional loss and seriously reduce the system efficiency.

As shown in Fig. 15, the operational characteristics of the proposed control strategy are captured. Even when the air gap varies, the phase difference between the primary current i_P and the secondary current i_S is fixed at 0.5π, indicating complete compensation on the secondary side, which proves the effectiveness of the secondary tuning control loop. Fig. 15(a)–(c) also shows the operating waveforms of the control angle φ of the primary and the secondary SCC and the conduction angle θ of the SAR, which conforms to the operating principle described in Section II-A. Moreover, soft-switching is enabled within the primary SCC, the secondary SCC, and the SAR. Primary input impedance is needed and utilized to facilitate a wide range of output power. As shown in Fig. 15(a)–(c), the phase of the v_P is ahead of the phase of the i_P, which ensures that the primary side is inductive reactance, and provides conditions for the full-bridge inverter to achieve ZVS.

The output power and dc-to-dc efficiency versus different air gaps under different cases are measured, as shown in Fig. 16. Without effective control strategies, the output power and efficiency of the system exhibited instability, as illustrated in the curves (marked with "□") in Fig. 16. The uncontrollable output power and reduced transmission efficiency significantly impacted the system's performance, leading to detrimental effects on the load. The curves (marked with "◯") in Fig. 16 represent the results after controlling. As the theoretical analysis in Section III-A and Section III-B, the secondary side completes the tuning and load matching control. Thus, by simultaneously satisfying (11) and (12), the system's efficiency remains at its optimum, which is 25.7% better than the traditional S/S compensation under the air gap $d = 80$ mm ($k = 0.1$). In addition, the output power of the system is tightly controlled at about 507 W, which is the same as the analysis in Section III-C, ensuring output stability by controlling the SCC control angle φ_P on the primary side.

To analyze the factors influencing system efficiency, power losses under different sets at the farthest air gap $d = 80$ mm ($k = 0.1$) are shown in Fig. 17. In the method without controlling, by measuring the four power parameters P_{in}, $P_{O,\text{inv.}}$, $P_{O,\text{LCT}}$, and P_O, the power loss of the system can be divided into three parts : $P_{\text{inv.}}$, P_{LCT}, and $P_{\text{rec.}}$. As shown in Fig. 17(a), with increasing air gap, both primary and secondary leakage inductances experience significant changes, leading to unavoidable system detuning. As M decreases, the system's input impedance decreases, $\mathbf{I}_P$ increases, resulting in increasing the losses in the inverter and resonant tank, which seriously damages the transmission efficiency. In Fig. 17(b), based on the proposed topology and control methodology, the power losses in inverter, primary SCC, coupling coil, secondary SCC, and SAR are denoted as $P_{\text{inv.}}$, $P_{P,\text{SCC}}$, P_{LCT}, $P_{S,\text{SCC}}$, and P_{SAR}, respectively. Benefiting from the tuning matching and optimal load tracking control are completed on the secondary side. The total loss of the system is reduced by 331 W and the efficiency is improved by 25.69%. Moreover, the utilization of reactive power on the primary side ensures the stability of the system's output.

To validate the proposed method can maintain optimal transmission efficiency and output stability over a wide load range,

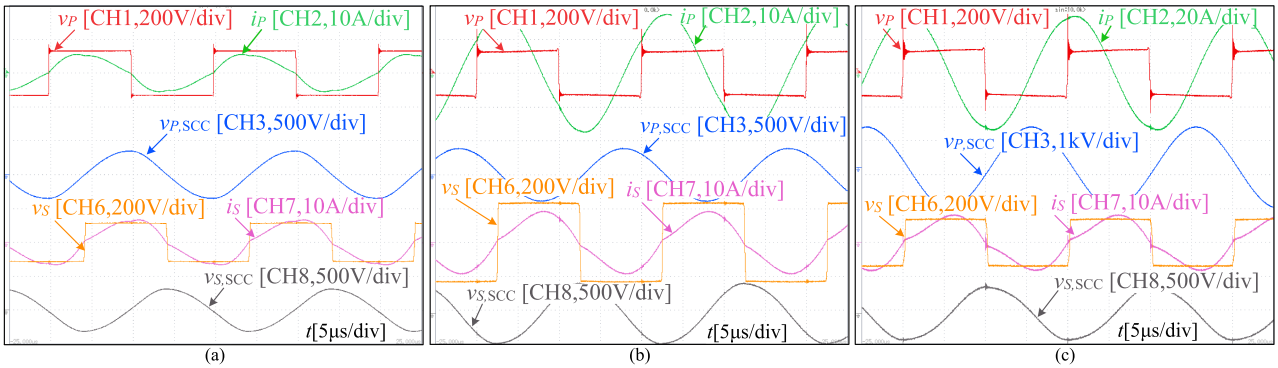

Fig. 14. Screenshots of steady-state waveforms without controlling (traditional S/S compensation topology) under different air gaps. (a) $d = 20$ mm ($k = 0.55$). (b) $d = 38$ mm ($k = 0.325$). (c) $d = 80$ mm ($k = 0.1$).

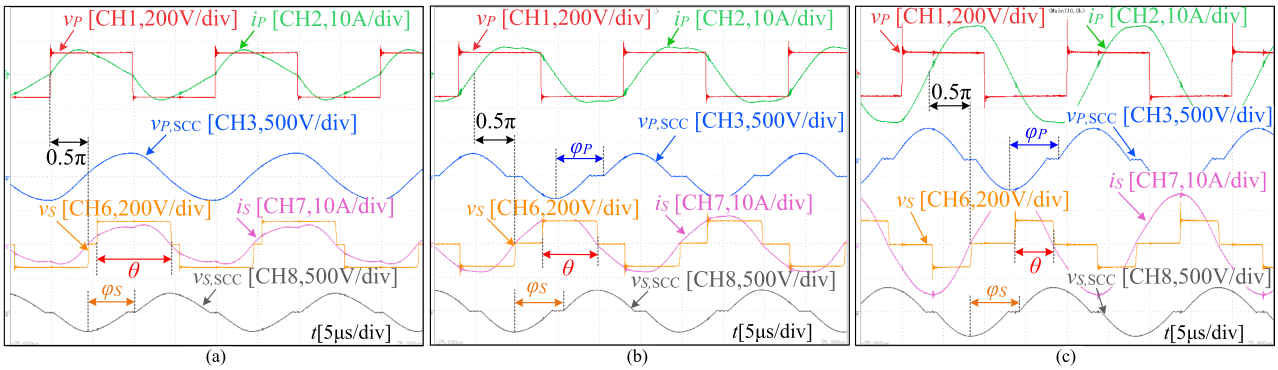

Fig. 15. Screenshots of steady-state waveforms after controlling (the proposed topology and mutiloop control method) under different air gaps. (a) $d = 20$ mm ($k = 0.55$). (b) $d = 38$ mm ($k = 0.325$). (c) $d = 80$ mm ($k = 0.1$).

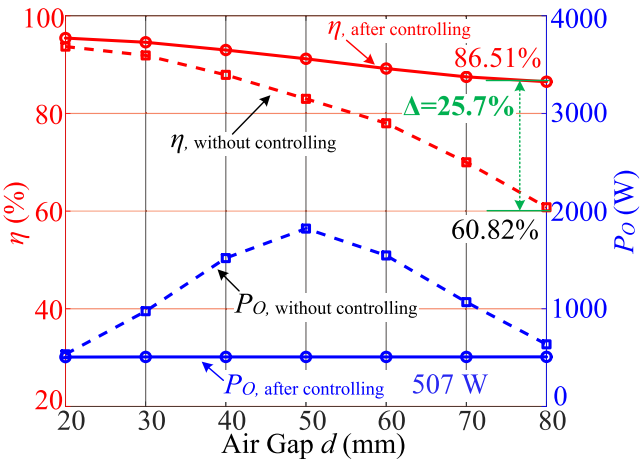

Fig. 16. Measured DC-to-DC efficiency η and output power P_O versus different air gaps under different cases.

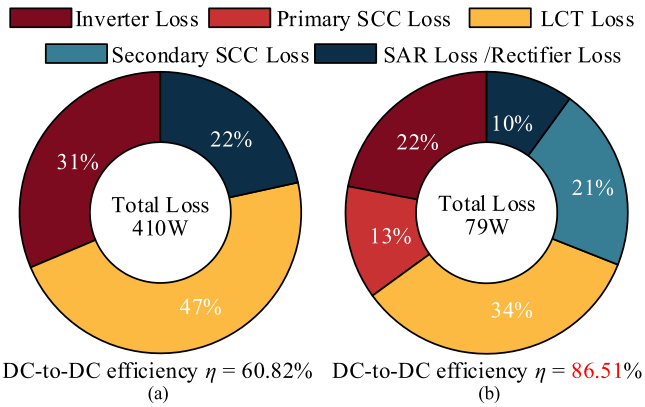

Fig. 17. Power loss under different cases with $d = 80$ mm ($k = 0.1$). (a) Without controlling. (b) After controlling.

the system output characteristics and dc-to-dc efficiency are measured when the air gap $d = 38$ mm ($k = 0.325$), as shown in Fig. 18. The corresponding output current (marked with "△") is inversely proportional to the output voltage (marked with "□"). The corresponding output power (marked with "◊") is approximately constant at 507 W. The maximum efficiency (marked with "◯") is maintained at around 93%, which is consistent with the analysis in Section III-D.

B. Transient Response of Gradient Descent Method for Secondary Tuning

This article proposes gradient descent method for secondary tuning to address variations in coupler parameters induced by

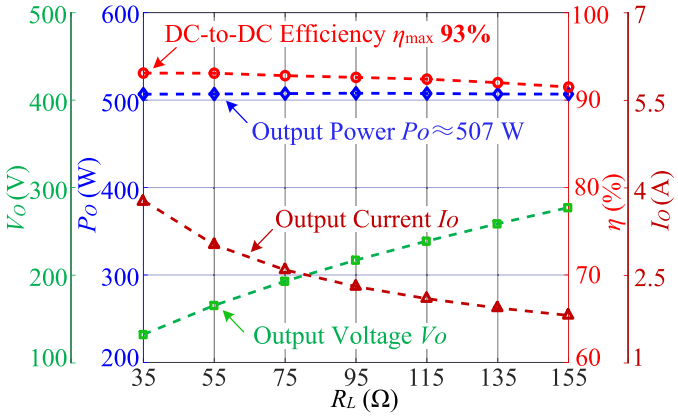

Fig. 18. Measured output characteristics and DC-to-DC efficiency of the system versus R_L.

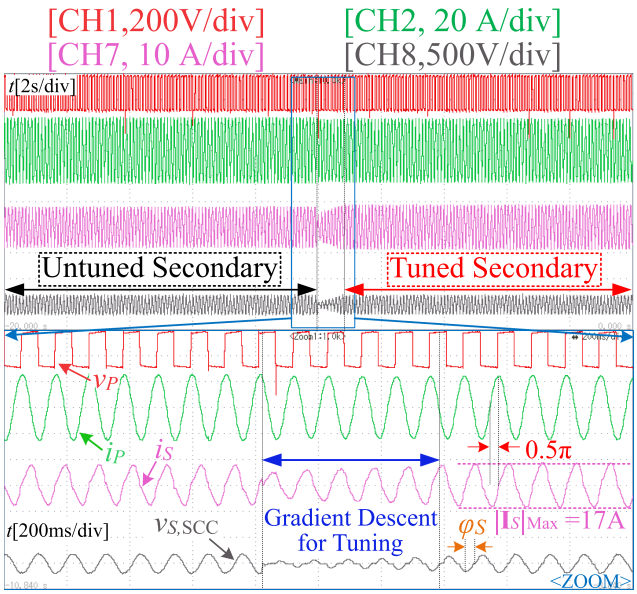

Fig. 19. Screenshots of transient response of gradient descent method for secondary tunning when air gaps $d = 80$ mm ($k = 0.1$).

misalignment, aiming for a simpler and more intuitive validation of its effectiveness. When the air gap $d = 80$ mm ($k = 0.1$), the comparative transient waveform of the proposed tuning method for the secondary side alone in an untuned system is captured, as shown in Fig. 19. In the initial stage, the secondary measurement reflects an untuned state, and through the ZOOM window, it can be seen that the steady-state waveform is consistent with Fig. 14. When the proposed gradient descent tuning method is suddenly added to the secondary side, it can be observed through the ZOOM window that the system continuously detects the magnitude $|\mathbf{I}_S|$ and adjusts the control angle φ_S of the secondary SCC accordingly until $|\mathbf{I}_S|$ is modulated to its maximum value $|\mathbf{I}_S|_{\text{Max}}$, and the system maintains the φ_S. From the ZOOM window waveform of the tuned secondary, it is easy to compare the phase of i_P and i_S, which remains fixed at 0.5π, indicating that the secondary side of the system has reached resonance condition, as described in Section III-A.

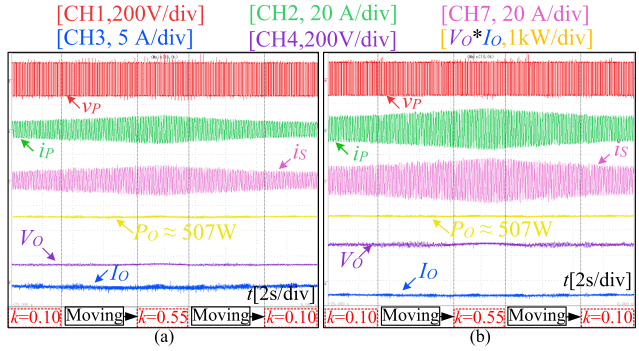

Fig. 20. Transient waveforms against variation of air gap under different loads. (a) $R_L = 35\,\Omega$. (b) $R_L = 155\,\Omega$.

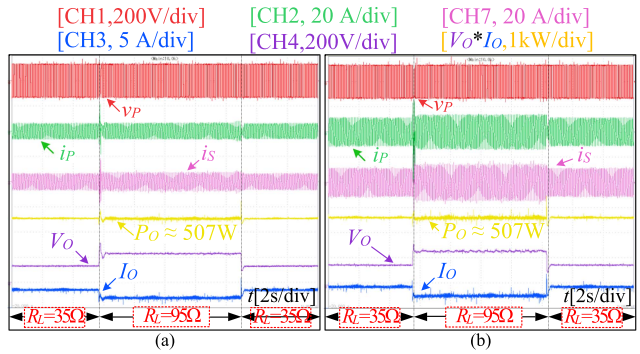

Fig. 21. Transient waveforms against step load change under different air gaps. (a) $d = 20$ mm ($k = 0.55$). (b) $d = 80$ mm ($k = 0.1$).

C. Transient Response Against Variation of Air Gap

The transient waveforms against variation of air gap under different loads are shown in Fig. 20. The air gap varies from 20 mm to 80 mm and then back to 20 mm by slowly changing the displacement of the secondary pad to the primary pad. The ac voltage v_P and current i_P of the primary side, ac current i_S of the secondary side are measured, corresponding to CH1, CH2, and CH7, respectively. As shown in Fig. 20, although the amplitudes of $|\mathbf{I}_P|$ and $|\mathbf{I}_S|$ vary with the air gap, their ratio $\alpha = |\frac{\mathbf{I}_S}{\mathbf{I}_P}|$ remains constant, rigorously regulated to 1.0 to achieve optimal efficiency control, consistent with the theoretical analysis in Section III-B. In addition, the dc output current I_O and voltage V_O of the secondary side are measured, corresponding to CH3 and CH4, respectively. The system output power of the yellow MATH channel is obtained by multiplying V_O and I_O, the output power P_O can be strictly adjusted to $P_{O,\text{ref}} = 507$ W.

D. Transient Response Against Variation of Loads

Fig. 21 shows the transient waveform against step load change under different values of air gaps. The load resistance is step changed from 35 Ω to 95 Ω, and then returns to 35 Ω again. Through the tuning matching control of the secondary SCC, the maximum value of $|\mathbf{I}_S|$ is ensured. Simultaneously, the amplitude ratio α of $|\mathbf{I}_P|$ and $|\mathbf{I}_S|$ remains constant and is strictly adjusted to 1.0 by the optimal load tracking control on

the secondary SAR, consistent with the theoretical analysis of Section III-A and III-B. The output power P_O is tightly regulated to 507 W by controlling the primary SCC. The experimental results demonstrate fast system response and high stability.

The proposed system demonstrates the robustness and optimal efficiency against misalignment and detuning across various air gaps and load conditions, making it highly valuable for widespread application and industrial implementation of wireless charging technology.

V. Conclusion

This article aims to address the challenges of achieving optimal efficiency tracking and output stability in the presence of variations in air gaps and load conditions. A power-source single-stage IPT system with two SCCs and a SAR is introduced. Based on this topology, a multiloop control strategy is employed that obviates the need for detecting changes in the loosely coupled parameters. On the secondary side, a combination of gradient descent method for secondary tuning and optimal load matching control is applied to achieve optimal efficiency transmission. Moreover, the stability of the system output is ensured through regulating power control on the primary side. In addition, all switches operate at a fixed frequency and achieve soft switching. Extensive experimental validation utilizing a 500 W prototype is conducted, including comparative experiments, steady-state waveforms, and transient responses, to verify the performance and advantages of the proposed system. Experimental results indicate that as the air gap increases from 20 to 80 mm, the system efficiency ranges from 95.45% to 86.51%, with self-inductance and mutual inductance increasing by 9.5% and 450%, respectively.

References

[1] G. A. Covic and J. T. Boys, "Inductive power transfer," *Proc. IEEE*, vol. 101, no. 6, pp. 1276–1289, Jun. 2013.

[2] A. Mahesh, B. Chokkalingam, and L. Mihet-Popa, "Inductive wireless power transfer charging for electric vehicles–A review," *IEEE Access*, vol. 9, pp. 137667–137713, 2021.

[3] D. Patil, M. K. McDonough, J. M. Miller, B. Fahimi, and P. T. Balsara, "Wireless power transfer for vehicular applications: Overview and challenges," *IEEE Trans. Transport. Electrific.*, vol. 4, no. 1, pp. 3–37, Mar. 2018.

[4] Y. Chen, H. Zhang, C. S. Shin, C. H. Jo, S. J. Park, and D. H. Kim, "An efficiency optimization-based asymmetric tuning method of double-sided LCC compensated WPT system for electric vehicles," *IEEE Trans. Power Electron.*, vol. 35, no. 11, pp. 11475–11487, Nov. 2020.

[5] X. Li, C. Wang, H. Wang, X. Dai, Y. Sun, and A. P. Hu, "A robust wireless power transfer system with self-alignment capability and controllable output current for automatic-guided vehicles," *IEEE Trans. Power Electron.*, vol. 38, no. 10, pp. 11898–11906, Oct. 2023.

[6] F. Lu et al., "A tightly coupled inductive power transfer system for low-voltage and high-current charging of automatic guided vehicles," *IEEE Trans. Ind. Electron.*, vol. 66, no. 9, pp. 6867–6875, Sep. 2019.

[7] J. Wang, C. Wang, S. Zhang, H. Yuan, Q. Zhang, and D. Li, "Constant-current and constant-voltage output using hybrid compensated single-stage resonant converter for wireless power transfer," *IEEE J. Emerg. Sel. Topics Power Electron.*, vol. 10, no. 5, pp. 6371–6382, Oct. 2022.

[8] C. R. Teeneti, T. T. Truscott, D. N. Beal, and Z. Pantic, "Review of wireless charging systems for autonomous underwater vehicles," *IEEE J. Ocean. Eng.*, vol. 46, no. 1, pp. 68–87, Jan. 2021.

[9] Y. Zhang, S. Chen, X. Li, and Y. Tang, "Design methodology of free-positioning nonoverlapping wireless charging for consumer electronics based on antiparallel windings," *IEEE Trans. Ind. Electron.*, vol. 69, no. 1, pp. 825–834, Jan. 2022.

[10] Y. Chen et al., "Variable-parameter t-circuit-based IPT system charging battery with constant current or constant voltage output," *IEEE Trans. Power Electron.*, vol. 35, no. 2, pp. 1672–1684, Feb. 2020.

[11] I. W. Iam et al., "Constant-frequency and noncommunication-based inductive power transfer converter for battery charging," *IEEE J. Emerg. Sel. Topics Power Electron.*, vol. 10, no. 2, pp. 2147–2162, Apr. 2022.

[12] Z. Huang, B. Zou, Z. Huang, H. H. C. Iu, and C. K. Tse,, "A single-stage IPT converter with optimal efficiency tracking and constant voltage output against dynamic variations of coupling and load," *IEEE Trans. Transp. Electrific.*, early access, May 31, 2024, doi: 10.1109/TTE.2024.3407717.

[13] C. Zhang, W. Lu, J. Zhao, X. Wu, H. Chen, and D. Xu., "A novel asymmetric magnetic coupler applied to multiple-receiver wireless charging system for automated guided vehicles," *IEEE Trans. Power Electron.*, vol. 38, no. 11, pp. 14761–14775, Nov. 2023.

[14] A. Ahmad, M. S. Alam, and R. Chabaan, "A comprehensive review of wireless charging technologies for electric vehicles," *IEEE Trans. Transp. Electrific.*, vol. 4, no. 1, pp. 38–63, Mar. 2018.

[15] J. S. Choi, S. Y. Jeong, B. G. Choi, S.-T. Ryu, C. T. Rim, and Y.-S. Kim, "Air-gap-insensitive IPT pad with ferromagnetic and conductive plates," *IEEE Trans. Power Electron.*, vol. 35, no. 8, pp. 7863–7872, Aug. 2020.

[16] B. Yang et al., "Analysis and design of a t/s compensated IPT system for AGV maintaining stable output current versus air gap and load variations," *IEEE Trans. Power Electron.*, vol. 37, no. 5, pp. 6217–6228, May 2022.

[17] J. Hou, Q. Chen, S. C. Wong, C. K. Tse, and X. Ruan, "Analysis and control of series/series-parallel compensated resonant converter for contactless power transfer," *IEEE J. Emerg. Sel. Topics Power Electron.*, vol. 3, no. 1, pp. 124–136, Mar. 2015.

[18] B. Yang et al., "A design method to minimize detuning for double-sided LCC-compensated IPT system improving efficiency versus air gap variation," *IEEE Trans. Power Electron.*, vol. 39, no. 1, pp. 1723–1737, Jan. 2024.

[19] Q. Wang et al., "Inductive power transfer system with constant current-constant voltage charging tolerating misalignment based on multi-objective optimization for compensation topology," *IEEE Trans. Power Electron.*, vol. 40, no. 3, pp. 4581–4591, Mar. 2025, doi: 10.1109/TPEL.2024.3435424.

[20] Y. Jia, Z. Wang, C. Tang, L. Zhao, X. Li, and C. Wang, "An efficiency improvement method for the small air gap wireless power transfer system with variable parameters," *IEEE Trans. Power Electron.*, vol. 38, no. 11, pp. 13443–13453, Nov. 2023.

[21] Y. Zhang, T. Kan, Z. Yan, and C. C. Mi, "Frequency and voltage tuning of series–series compensated wireless power transfer system to sustain rated power under various conditions," *IEEE J. Emerg. Sel. Topics Power Electron.*, vol. 7, no. 2, pp. 1311–1317, Jun. 2019.

[22] G. Guidi and J. A. Suul, "Minimizing converter requirements of inductive power transfer systems with constant voltage load and variable coupling conditions," *IEEE Trans. Ind. Electron.*, vol. 63, no. 11, pp. 6835–6844, Nov. 2016.

[23] T. C. Beh, M. Kato, T. Imura, S. Oh, and Y. Hori, "Automated impedance matching system for robust wireless power transfer via magnetic resonance coupling," *IEEE Trans. Ind. Electron.*, vol. 60, no. 9, pp. 3689–3698, Sep. 2013.

[24] H. Zhang, Y. Chen, D. H. Kim, Z. Li, M. Zhang, and G. Li, "Variable inductor control for misalignment tolerance and constant current/voltage charging in inductive power transfer system," *IEEE J. Emerg. Sel. Topics Power Electron.*, vol. 11, no. 4, pp. 4563–4573, Aug. 2023.

[25] Z. Li, H. Liu, Y. Huo, J. He, Y. Tian, and J. Liu, "High-misalignment tolerance wireless charging system for constant power output using dual transmission channels with magnetic flux controlled inductors," *IEEE Trans. Power Electron.*, vol. 37, no. 11, pp. 13930–13945, Nov. 2022.

[26] B. Zou and Z. Huang, "Primary-frequency-tuning and secondary-impedance-matching IPT converter with programmable constant power output and optimal efficiency tracking against variation of coupling coefficient," *IEEE Trans. Power Electron.*, vol. 39, no. 4, pp. 4895–4909, Apr. 2024.

[27] Z. Huang, C. S. Lam, P. I. Mak, R. P. D. S. Martins, S. C. Wong, and C. K. Tse, "A single-stage inductive-power-transfer converter for constant-power and maximum-efficiency battery charging," *IEEE Trans. Power Electron.*, vol. 35, no. 9, pp. 8973–8984, Sep. 2020.

[28] D. H. Kim and D. Ahn, "Self-tuning LCC inverter using PWM-controlled switched capacitor for inductive wireless power transfer," *IEEE Trans. Ind. Electron.*, vol. 66, no. 5, pp. 3983–3992, May 2019.
[29] W. Li, G. Wei, C. Cui, X. Zhang, and Q. Zhang, "A double-side self-tuning LCC/S system using a variable switched capacitor based on parameter recognition," *IEEE Trans. Ind. Electron.*, vol. 68, no. 4, pp. 3069–3078, Apr. 2021.
[30] Z. Luo, Y. Zhao, M. Xiong, X. Wei, and H. Dai, "A self-tuning LCC/LCC system based on switch-controlled capacitors for constant-power wireless electric vehicle charging," *IEEE Trans. Ind. Electron.*, vol. 70, no. 1, pp. 709–720, Jan. 2023.
[31] K. Colak, E. Asa, M. Bojarski, D. Czarkowski, and O. C. Onar, "A novel phase-shift control of semibridgeless active rectifier for wireless power transfer," *IEEE Trans. Power Electron.*, vol. 30, no. 11, pp. 6288–6297, Nov. 2015.
[32] Z. Huang, S. C. Wong, and C. K. Tse, "An inductive-power-transfer converter with high efficiency throughout battery-charging process," *IEEE Trans. Power Electron.*, vol. 34, no. 10, pp. 10245–10255, Oct. 2019.
[33] W. Gu and K. Harada, "A new method to regulate resonant converters," *IEEE Trans. Power Electron.*, vol. 3, no. 4, pp. 430–439, Oct. 1988.

Bowei Zou (Graduate Student Member, IEEE) received the B.Eng. degree in electrical and intelligent engineering and the M.Eng. degree in electrical engineering from Xiangtan University, Xiangtan, China, in 2018 and 2021, respectively. He is currently working toward the Ph.D. degree in power electronics with the Shien-Ming Wu School of Intelligent Engineering, South China University of Technology, Guangzhou, China.

His current research interests include wireless power transfer and power electronics.

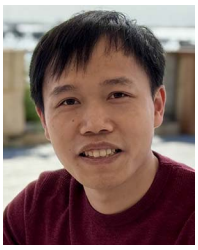

Zhicong Huang (Senior Member, IEEE) received the B.Eng. degree in electrical engineering and automation and the M.Eng. degree in mechanical and electronic engineering from the Huazhong University of Science and Technology, Wuhan, China, in 2010 and 2013, respectively, and the Ph.D. degree in power electronics from the Hong Kong Polytechnic University, Hong Kong, in 2018.

In 2019, he was a Postdoctoral Fellow under the UM Macao Talent Program with the State Key Laboratory of Analog and Mixed-Signal VLSI, Macau, China. Since 2020, he has been an Associate Professor with the Shien-Ming Wu School of Intelligent Engineering, South China University of Technology, Guangzhou, China. His research interests include wireless power transfer, artificial intelligence in power electronics, and wave energy converters.

Dr. Huang was the recipient of the Outstanding Reviewer Award for IEEE TRANSACTIONS ON POWER ELECTRONICS in 2021, the Star Reviewer Award for IEEE JOURNAL ON EMERGING AND SELECTED TOPICS IN POWER ELECTRONICS in 2023, and the Best Reviewer for IEEE JOURNAL ON EMERGING AND SELECTED TOPICS IN CIRCUITS AND SYSTEMS in 2023.

Io-Wa Iam (Member, IEEE) received the B.Sc. and Ph.D. degrees in electrical and computer engineering from the University of Macau, Macau, China, in 2020 and 2023, respectively.

His current research interests include power electronics and wireless power transfer.

Dr. Iam was the recipient of the "Best Track Paper Award" in IEEE APPEEC 2019.

Chi-Seng Lam (Senior Member, IEEE) received the Ph.D. degree in electrical and electronics engineering from the University of Macau (UM), Macau, China, in 2012, and the Clare Hall Study Programme in power electronics from the University of Cambridge, Cambridge, U.K., in 2019.

In 2013, he was a Postdoctoral Fellow with The Hong Kong Polytechnic University, Hong Kong, China. He is currently an Associate Professor with the State Key Laboratory of Analog and Mixed-Signal VLSI and the Institute of Microelectronics, UM, and also with the Department of Electrical and Computer Engineering, Faculty of Science and Technology, UM. He has coauthored or coedited four books and more than 190 technical journals and conference papers. He holds six US and six Chinese patents. His research interests include power quality compensators, photovoltaic energy generation system, power management integrated circuits, and wireless power transfer.

Dr. Lam was the recipient or co-recipient of the IEEE PES Chapter Outstanding Engineer Award in 2016, the Gold Medal of the 48th Geneva International Exhibition of Inventions in 2023, and the Macao Science and Technology Invention Award (third class and second class) in 2014 and 2018, respectively. He is currently the Chair of the Young Professionals in Circuits and Systems (YPCAS) of IEEE CASS, Founding Chair of the IEEE Macau IES Chapter, and the Secretary of the IEEE IES Technical Committee on Power Electronics. He is currently an Associate Editor for IEEE TRANSACTIONS ON POWER ELECTRONICS, IEEE TRANSACTIONS ON INDUSTRIAL ELECTRONICS, IEEE JOURNAL OF EMERGING AND SELECTED TOPICS IN POWER ELECTRONICS, IEEE OPEN JOURNAL OF THE INDUSTRIAL ELECTRONICS SOCIETY, and IEEE ACCESS. He was awarded 2021 IEEE ACCESS Outstanding Associate Editor and the 2022 IEEE TRANSACTIONS ON INDUSTRIAL ELECTRONICS Distinguished Reviewer.